HHS Public Access

Author manuscript

ACS Nano. Author manuscript; available in PMC 2018 June 27.

Published in final edited form as:

ACS Nano. 2017 June 27; 11(6): 5623–5632. doi:10.1021/acsnano.7b01006.

Oxygen Sensing with Perfluorocarbon-Loaded Ultraporous Mesostructured Silica Nanoparticles

Amani L. Lee[†,%], **Clifford T. Gee**[†,%], **Bradley P. Weegman**[‡], **Samuel A. Einstein**[‡], **Adam Juelfs**[†], **Hattie L. Ring**[‡,†], **Katie R. Hurley**[†], **Sam M. Egger**[†], **Garrett Swindlehurst**[§], **Michael Garwood**[‡], **William C. K. Pomerantz**[*,†], and **Christy L. Haynes**[*,†]

[†]Department of Chemistry, University of Minnesota, Minneapolis, MN 55455, United States

[§]Department of Chemical Engineering & Material Science, University of Minnesota, Minneapolis, MN 55455, United States

[‡]Center for Magnetic Resonance Research, University of Minnesota, Minneapolis, MN 55455, United States

Abstract

Oxygen homeostasis is important in the regulation of biological function. Disease progression can be monitored by measuring oxygen levels, thus producing information for the design of therapeutic treatments. Non-invasive measurements of tissue oxygenation require the development of tools with minimal adverse effects and facile detection of features of interest. Fluorine magnetic resonance imaging (^{19}F-MRI) exploits the intrinsic properties of perfluorocarbon (PFC) liquids for anatomical imaging, cell tracking, and oxygen sensing. However, the highly hydrophobic and lipophobic properties of perfluorocarbons require the formation of emulsions for biological studies. Though, stabilizing these emulsions has been challenging. To enhance the stability and biological loading of perfluorocarbons, one option is to incorporate perfluorocarbon liquids into the internal space of biocompatible mesoporous silica nanoparticles. Here, we developed perfluorocarbon-loaded ultraporous mesostructured silica nanoparticles (PERFUMNs) as ^{19}F-MRI detectable oxygen sensing probes. Ultraporous mesostructured nanoparticles (UMNs) have large internal cavities (average = 1.76 $cm^3\ g^{-1}$), facilitating an average 17% loading efficiency of PFCs, meeting the threshold fluorine concentrations needed for imaging studies. Perfluoro-15-crown-5-ether PERFUMNs have the highest equivalent nuclei per PFC molecule, and a spin-lattice (T_1) relaxation-based oxygen sensitivity of 0.0032 $mmHg^{-1}\ s^{-1}$ at 16.4 T (657 MHz). The option of loading PFCs after synthesizing UMNs, rather than the more traditional *in situ* core-shell syntheses, allows for use of a broad range of PFC liquids from a single material. The

[*]**Corresponding Author**: wcp@umn.edu, chaynes@umn.edu.

[%]These authors contributed equally.

ASSOCIATED CONTENT

Supporting Information is available free of charge *via* the Internet at http://pubs.acs.org.

Calculations of loading efficiency, table of PERFUMN T_1 values, additional N_2 physisorption characterization, additional TEM and Cryo-TEM images of UMNs and PERFUMNs, images of PERFUMN extraction, DLS polydispersity comparison, comparison of DLS and TEM size characterizations, full ^{19}F NMR spectra of PERFUMNs, ^{19}F NMR evaluation of line broadening and chemical shifts, PERFUMN loading variability data, temperature dependence of PFCE-PERFUMNs, ^{19}F MRI SNR analysis, relaxation rates of PFCE-PERFUMNs in whole blood, oxygen sensitivity in whole blood, images of whole blood integrity.

Author Contributions

The manuscript was written through contributions of all authors. All authors have given approval to the final version of the manuscript.

biocompatible and tunable chemistry of UMNs combined with the intrinsic properties of PFCs makes PERFUMNs a MRI sensor with potential for anatomical imaging, cell tracking, and metabolic spectroscopy with improved stability.

Graphical Abstract

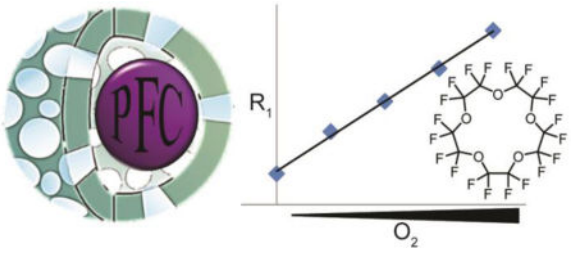

Keywords

perfluorocarbons; mesoporous silica nanoparticles; magnetic resonance; oximetry; relaxometry; thermometry

Oxygen homeostasis is vital for regulating biological function, including metabolism and disease progression.[1–5] In most cases hypoxic tumors are resistant to both radiation and many traditional chemotherapy treatments; researchers are developing combinatorial therapies, as well as, agents activated by tumor hypoxia to treat cancer.[6–8] Additionally, pathogenic infections are highly sensitive to the oxygen level.[4, 5] Better measurements of oxygen levels in these tissue microenvironments are needed to optimize oxygen-dependent therapies. Given the significance of tissue oxygenation, many researchers have sought to develop efficient and sensitive technologies for oximetry measurements.[9] However, current oximeters tend to be invasive, consume oxygen, or are limited to superficial measurements.[4, 10] The combination of fluorine-19 magnetic resonance imaging (^{19}F-MRI) and biocompatible nanomaterials reported herein has the potential to be an effective platform for *in situ* oxygen detection.

Non-invasive oximetry methods that measure oxygen levels are currently being explored for clinical applications. Magnetic resonance is a method that uses electromagnetic radiation to probe systems without a limitation in tissue penetration. Techniques such as electron paramagnetic resonance (EPR) spectroscopy, nuclear magnetic resonance (NMR) spectroscopy, magnetic resonance imaging (MRI), and magnetic resonance spectroscopy (MRS) are able to detect the levels of oxygen under strong magnetic fields.[11, 12] EPR is a spectroscopic technique that can detect species with unpaired electrons.[13] Clinically approved EPR spectrometers are being developed and optimized with careful considerations of the microwave radiation needed for excitation.[14–17] Alternatively, MRI and NMR detect signals from NMR-active nuclei. For *in vivo* oximetry, ^{19}F-MRI and fluorine-19 MRS (^{19}F-MRS), using highly fluorinated materials, are particularly attractive approaches and have already been used for enhanced imaging[18, 19], cell tracking[20], and probing the microenvironments of tissue.[21]

The ^{19}F nucleus is 100% naturally abundant, has a high gyromagnetic ratio (γ = 40.05 MHz/T), and is highly responsive to changes in its chemical environment. The use of ^{19}F nuclei is also advantageous due to the lack of endogenous fluorine and thus, background noise.[22, 23] In ^{19}F-MRI, partially or perfluorinated compounds (*i.e.*, perfluorocarbons, PFCs), commonly used as contrast agents, have the capacity to dissolve high amounts of gases (*e.g.*, O_2, N_2, and CO_2).[24–26] Upon dissolution into the PFC, the presence of O_2 changes the spin-lattice relaxation time constant (T_1) of the ^{19}F nuclei, based on dipole-dipole interactions between the ^{19}F nucleus and the O_2 unpaired electrons, which is detected by NMR in a concentration-dependent manner. PFCs used for oxygen sensing or delivery have been established in the literature, including: perfluoro-15-crown-5-ether (PFCE), hexafluorobenzene (HFB), perfluorodecalin (PFD), perfluorooctyl bromide (PFOB), perfluoro(tert-butylcyclohexane) (PFTBCH), and perfluorotributylamine (PFTBA).[27–32]

The current state-of-art method for dispersing PFCs in aqueous media, as must be done for *in vivo* imaging, is the emulsification of PFCs with surfactants.[31, 33, 34] However, these emulsions can become unstable and lead to coalescence and Ostwald ripening, effectively restricting homogenous dispersion of the probe.[35, 36] To increase the colloidal stability and homogenous distribution, recent studies have encapsulated PFCs into biocompatible mesoporous silica nanoparticles (MSNs). The advantages of MSNs are their controllable pore size and surface chemistry; their internal space is suitable for loading cargo of interest, and their surfaces can be modified with biological targeting moieties. Chin *et al.* reports a silica nanocapsule filled with PFD for ultrasound measurements.[37] Thermogravimetric analysis and ^{19}F-NMR showed that 78 wt % of particles consisted of PFD, while the remaining mass consisted of the silica shell. While the silica nanocapsule stabilized the PFD, in comparison to the emulsion, the colloids destabilized completely after 24 hours. Nakamura *et al.*[38] reported a PFC core-shell MSN called mFLAME filled with PFCE for drug delivery. The mFLAME particles were modified with different surface ligands which allowed for dual mode detection using ^{19}F-MRI and fluorescence microscopy. The authors were able to obtain *in vitro* ^{19}F-MR images from 2 mM PFCE concentration at 11.7 T with an acquisition time of approximately 30 minutes (1820 seconds). They also obtained *in vivo* measurements in a mouse model with an acquisition time as fast as 250 seconds. However, the core-shell structure limits both the amount and versatility of loadable PFC per nanoparticle.

Here, we are evaluating the loading capacity of ultraporous mesostructured silica nanoparticles (UMNs) as an alternative material for ^{19}F-MRI. The insensitivity of MRI requires high concentrations of fluorine to overcome the detection limit. It is estimated that 30 mM of ^{19}F may be needed for clinical application (≤ 3 T).[19] Thus, the loading capacity of MSNs and the PFC fluorine density need careful consideration. The current MSNs have pore volumes much lower than 2 $cm^3\ g^{-1}$, limiting the volume of PFCs that can be loaded. We recently reported on the synthesis of UMNs, spherical MSNs that feature pore volumes up to 4.5 $cm^3\ g^{-1}$.[39] The surfaces of UMNs are readily modified with polyethylene glycol (PEG) and chlorotrimethylsilane (TMSCl) to improve their colloidal stability and biocompatibility as biologically inert vehicles. Given their comparatively high pore volume, stability under a variety of conditions, and prior precedent with silica nanoparticles, these particles were selected as an ideal candidate for loading with perfluorocarbons.

In this study, we developed perfluorocarbon-loaded ultraporous mesostructured silica nanoparticles (PERFUMNs) as ^{19}F-MRI-detectable oxygen sensing probes. We assessed the loading efficiency of PERFUMNs loaded with three different PFCs, with ^{19}F-NMR spectroscopy and compared the performance to using existing MSNs. As our initial attempt to study our fluorinated contrast agents in a biologically relevant context, we evaluated the PERFUMNs stability in whole blood over several days. Lastly, we demonstrated the sensitivity of PERFUMNs to oxygen with ^{19}F-NMR relaxometry.

Results and Discussion

Synthesis and Characterization of Dual-modified UMNs

To achieve optimal colloidal and hydrolytic stability, we modified the surface functionality of our mesoporous nanoparticles. The dual-modified UMNs were successfully synthesized *via* the sol-gel method.[40–42] The UMN surfaces were modified with PEG-silane, containing heterogeneous mixture with 9 to 12 repeating units, and TMSCl to increase the nanoparticle colloidal stability. The PEG-silanes are hydrophilic moieties that aid in dispersion of particles in aqueous media and reduction of non-specific protein adsorption.[43] The hydrophobic trimethylsilyl group protects the particles from hydrolysis reactions in aqueous environments.[44] A descriptive statistical analysis of the UMN physical properties was carried out between 15 different batches of dual-modified UMNs (Table 1).

Dynamic light scattering (DLS) reported a polydispersity index (PDI) of 0.11 ± 0.06. A PDI < 0.2 indicates that the size distribution of the particles is moderately uniform.[45] The zeta potential of the various batches of UMNs was measured with a range of −25 mV to −50 mV, indicating a suitable surface charge for colloidal stability. A significant difference between the dual-modified UMNs and the previously reported bare UMN nanoparticles is the pore volume and surface area. The Barrett-Joyner-Halenda (BJH) pore volume and surface area for bare UMNs were greater than 4 $cm^3\ g^{-1}$ and 1100 $m^2\ g^{-1}$, while the modified UMNs are 1.8 ± 0.3 $cm^3\ g^{-1}$ and 532.4 ± 74.9 $m^2\ g^{-1}$ respectively. This reduction in pore size can be explained due to the pore volume and nanoparticle surface area occupied by the modifying ligands.

The pore volumes of UMNs, compared to traditional MSNs, are on the higher end of the pore volume limit. The 95% confidence interval indicates that UMNs are capable of overcoming pore volumes of 2 $cm^3\ g^{-1}$. The average pore volume can be shifted based on the stoichiometry and type of surface modification moieties.[43] Furthermore, many MSNs have lower pore volumes due to the limited space from internal pore tunnels.[46] In comparison, UMNs have a large internal cavity allowing better packing in the open space.

Analysis of the N_2 physisorption isotherm (Figure 1A) shows that UMNs have a type IV isotherm with a type 5 (H5) hysteresis loop. Type IV isotherms are indicative of mesoporous particles, and H5 loops indicate presence of both open and blocked pores.[47] The hysteresis is likely a feature due to the difference in desorption between different pores. The BJH pore size analysis shows a bimodal distribution for the UMN population (Figure S1), in support that the UMNs contain surface pores and a large internal cavity.

Transmission electron microscopy (TEM) analysis shows a difference in mass-thickness contrast between the center and edges of unloaded UMNs, indicating hollow or lacey silica network in the center (Figure 1B, Figure S2A–C). Image analysis of the UMNs (n = 750) revealed average particle diameters of 122 ± 32 nm, with a silica shell thickness of 22 ± 21 nm. These values support the diameter found by DLS (142 nm). In our previous study with bare UMNs, scanning electron microscopy analysis revealed a spherical 3D–structure with raspberry-like surface textures.[39]

Loading and Characterization of PERFUMNs

PERFUMNs were made by loading UMNs *via* sonication with different types of PFCs: PFCE, PFD, and PFTBCH. PERFUMNs were extracted into an ultrapure water phase after vortexing the sample. The PEG-silanes on the surface of the PERFUMNs promote the particle extraction from the liquid PFC layer. During the extraction, the aqueous phase became turbid after complete phase separation while the liquid PFC phase became clear (Figure S3).

A two-tailed paired t-test shows all PERFUMNs demonstrated an increase of ≥ 30% in their effective diameter ($p = 0.023$) relative to their unloaded counterparts (Figure 1C). This measured increase is likely a result of the increased mass and change in refractive index from the addition of highly dense liquid PFC. The same test did not reveal significant difference in uniformity between PERFUMNs and unloaded UMNs (Figure S4). This would suggest that the extraction of PERFUMNs is not selective to a narrow size range of nanoparticles. Cryo-TEM images show the internal space of the UMNs have been packed with an atomically heavy substance (Figure 1D, Figure S2D–F). The mechanisms that control electron microscopy contrast are mass-thickness, diffraction, and phase contrast.[48, 49] Because fluorine atoms have the second highest atomic mass after silica atoms in these PERFUMNS, the contrast in the internal space of PERFUMNs, compared to unloaded UMNs, demonstrates the high concentration of fluorine atoms in the nanoparticles.

Since electron microscopy is a complementary technique for particle characterization it can help explain differences found in DLS. The DLS hydrodynamic diameters are sensitive to interparticle interactions (*e.g.*, electrostatic repulsion, van der Waals forces, and absorbed polymers) and the change in diffusion, leading to an overestimation of the particle diameter.[50] Additionally, UMNs with PFCs will change the effective particle density which will affect the particle diffusion. Slower diffusion leads to larger particle size in DLS. Thus, the physical diameters from DLS were compared to measurements from TEM and Cryo-TEM. No significant difference was found between the DLS effective diameter and both electron microscopy diameter measurements (Figure S5A). The lack of difference shows that the physical diameters of the particles remain the same, but is supportive that DLS distinguishes UMNs from PERFUMNs based on particle behavior.

Analysis of the particle size distributions (PSDs) shows both TEM (UMNs) and Cryo-TEM (PERFUMNs) have a unimodal distribution with a right skew (Figure S5B). The PDI is the squared quotient between the full width at half-maximum height and the mean of the PSDs ($[\text{width/mean}]^2$).[45] The PSDs of TEM and Cryo-TEM have PDIs of 0.263 and 0.335 respectively. The decrease in the uniformity can be expected for electron microscopy

techniques due to their low sample size, relative to the nanoparticle population, static conditions, and high vacuum environment.[49, 51] Together, these data demonstrate that dual functionalized UMNs can be synthesized with a large pore volume that is easily filled with PFCs. This success inspired further studies for ^{19}F-NMR and MRI behavior.

^{19}F-NMR Quantification of PERFUMN Loading

The loading capacity of the PERFUMNs was calculated through quantitative NMR. For maximizing ^{19}F-MRI signal sensitivity, it is necessary to take into account not only the amount of perfluorocarbon loaded into the nanoparticles but also how much signal each sample provides per magnetically-equivalent fluorine atom. For the materials under study here, PFCE contains 20 equivalent fluorines, PFTBCH contains 9 equivalent fluorines, while PFD contains 4 equivalent fluorines.[52, 53] PERFUMNs were loaded in triplicate, and spectra for each PERFUMN were obtained (Figure 2, Figure S6). The three different PERFUMNs, loaded with the PFCs above, were compared by the amount of fluorine per mass of nanoparticles (Figure 2 Inset). Importantly, confinement in our UMNs does not affect the linewidths of the observed fluorine resonances compared with the neat PFC resonances, supporting a highly mobile liquid phase within the UMNs (Figure S6). The PFCE-PERFUMNs had significantly higher loading than PFD-PERFUMNs ($p < 0.05$) and loaded five times more than PFCE filled MSNs ($p < 0.05$). The variation of the fluorine loading values of PFTBCH-PERFUMNs made them indistinguishable from the other three samples. Of note, the groups had different sample sizes, 3:6:9:3, from left to right respectively. However the one-way ANOVA has some power to account for unequal variances.

Sources of variability could be reflected in both the pore volume distribution of our UMNs and variability of the loading procedure itself. Cryo-TEM shows nano-sized bubbles (Figure S2) in the PERFUMNS, indicating incomplete loading of the UMN cavities. To evaluate the experimental variability in loading, two batches of PFCE-PERFUMNs (Batch X, Y) were loaded in triplicate to compare loading variability. Batch × had the highest loading variability with a coefficient of variation (CV) of 87.6%; Batch Y had a CV of 31.2% (Figure S8). There was no significant difference between Batch × and Batch Y. This variability in experimental loading suggests that it may be difficult to determine more subtle changes in loading during a complete analysis of loading conditions. Further differences in loading may be a result of the molecular packing of each PFC, but these effects are difficult to evaluate based on the current variability in our data. A complete analysis of the PFC physicochemical variants that affect molecular packing inside the UMN will be the focus of future PERFUMN experiments.

In addition to the fluorine content per nanoparticle, the PERFUMNs were also compared based on their loading yield and efficiency (Supplemental Information: “Calculations for PERFUMN Loading Yield & Efficiency”). The efficiency analysis of PFCE-PERFUMNs (n=6) shows a mean specific loading yield of 33% ± 21%, and mean efficiency is 15% ± 9% with typical nanoparticle concentrations of 0.4 mg UMNs/mL water. In comparison, PFCE filled MSNs (n=3) had an average yield of 14% ± 9% and efficiency of 1.3% ± 1%. These values indicate that improvements need to be investigated for the maximal filling of nanoparticle internal volume and the complete extraction of nanoparticles from the PFC

layer. However, an important facet of these loading data is that clinical MRI field strengths, as previously discussed, require around 30 mM fluorine to be detected, which is already achievable with these particles at a low nanoparticle concentration (~0.5 mg/mL).

PFC loaded nanoparticles can address that stability challenge of emulsions of PFCs, however the concentration of PFCs are lower and particle size dependent. In the context of a PFCE emulsion, Cabello *et al.* reported cationic and anionic emulsion particles with DLS diameters of 158 nm (0.119 PDI) and 207 nm (0.09 PDI) respectively.[19] In 8 μL volumes, the emulsion contained 4.8 mM of PFCE. This concentration corresponds to 38 nmol of PFCE (760 nmol of ^{19}F). In comparison, our PFCE-PERFUMNs, with a nanoparticle concentration of 1 mg mL^{-1}, would have 19 nmol PFCE (380 nmol ^{19}F). Although not stated in the manuscript, assuming the 4.8 mM corresponds to the anionic particles, then the 65 nm difference between their larger emulsion and our PERFUMNs led to a 2-fold increase in molar concentration of PFCE. Matushita *et al.*[54] have core-shell PFC filled MSNs synthesized around 80 nm emulsions of PFCE. In 0.5 mL they reported 1.3 mM PFCE; this corresponds to 0.65 μmol PFCE. In the same volume Cabello *et al.* would have 30 μmol PFCE, and our PERFUMNs would have 1.21 μmol PFCE. While increasing the size of the nanoparticles may seem desirable to obtain more fluorine per nanoparticle, the change in size may affect the colloidal stability or biodistribution of the UMNs.[55] As stated before, emulsions have to battle against coalescence and Ostwald ripening; the tradeoff for PFC concentration is the added stability of the UMNs.

Oxygen Sensitivity of PERFUMNs

The presence of pores on the surface of PERFUMNs makes the internal liquid PFCs accessible to molecular oxygen outside the nanostructures. As the oxygen dissolves into the liquid PFC, the dipole-dipole interactions between the fluorine nuclei and unpaired electrons of the oxygen reduce the T_1 relaxation times of the nuclei. Traditionally, T_1 values are determined using an inversion-recovery sequence. By measuring the T_1 at different partial pressures of oxygen (pO_2), the relaxation rate constant (R_1), or the inverse of the T_1, can be plotted as a function of pO_2 to give an oxygen calibration curve.[56] Figure 3 shows the R_1 as a function of pO_2 at 22 °C, 16.4 T (657 MHz). As expected, R_1 relaxation rates increase as the concentration of oxygen increases. The slopes and their error were determined with a linear regression fit. PFCE-PERFUMNs had a sensitivity to oxygen with a slope of 322 ± 4 (10^{-5} $mmHg^{-1}$ s^{-1}). PFTBCH-PERFUMNs had a sensitivity of 334 ± 3 (10^{-5} $mmHg^{-1}$ s^{-1}), and PFD-PERFUMNs had the lowest sensitivity of the three PERFUMNs described herein at 273 ± 3 (10^{-5} $mmHg^{-1}$ s^{-1}). To analyze the difference in sensitivities, an analysis of covariance was used to compare the slopes. There was a significant difference between the slopes ($p < 0.05$). A Newman-Keuls multiple comparison test, at a significance level of 0.01, revealed that PFD-PERFUMN sensitivity is significantly different from PFTBCH ($p < 0.0001$) and PFCE ($p < 0.0001$), while there is no significant difference between the most sensitive PERFUMNs loaded with PFTBCH and PFCE.

In our previous study, we report neat PFCE and PFD have a sensitivity of 223.4 ± 15 (10^{-5} $mmHg^{-1}$ s^{-1}) and 188.0 ± 38 (10^{-5} $mmHg^{-1}$ s^{-1}) respectively, at 16.4 T (37 °C).[57] During that study, we also found neat PFCE and PFD have a sensitivity of 280.4 ± 13 (10^{-5}

mmHg^{-1} s^{-1}) and 197.3 ± 31 (10^{-5} mmHg^{-1} s^{-1}) respectively, at 16.4 T, 22 °C (not reported). The trend in the intercepts of the PERFUMNs is consistent with the relationship of the inherent T_1 relaxation times between PFCE, PFD, and PFTBCH, where PFD has the longest T_1 relaxation time (Table S1). The PERFUMNs have a higher anoxic R_1 compared to neat PFC, indicating shorter T_1 relaxation times. The T_1 relaxation times are sensitive to the magnetic field, temperature, and the PFC microenvironment. In this case, the nanoparticles themselves could be affecting the relaxation of PFCs, likely due to both a decrease in molecular mobility of PFC inside of UMNs and the molecular interactions between the SiO_2 cage and PFC.[58, 59] Degradation of the silica nanoparticles may change the response curve of PFC to oxygen. As an initial evaluation of the PERFUMN stability, a preliminary analysis in whole blood is described in "PERFUMN Oxygen Measurements in Whole Blood".

Our previous study shows oxygen concentration, as well as temperature, can influence the R_1 relaxation rates of fluorine nuclei.[57] We have also shown this phenomenon with PFCE-PERFUMNs (Figure S9). As the temperature increased (22 to 45 °C) the O_2 sensitivity of the PFCE-PERFUMNs dropped from 322 (10^{-5} mmHg^{-1} s^{-1}) to 161 (10^{-5} mmHg^{-1} s^{-1}). The anoxic R_1 (0 mmHg O_2) shows PFCE-PERFUMNs have a sensitivity of −226 (10^{-4} °C^{-1} s^{-1}). If the error in temperature is ± 1 °C, this could change the sensitivity in oxygen by 7 (10^{-5} mmHg^{-1} s^{-1}). The variability in temperature, similar to *in vivo* conditions, adds to the uncertainty in oxygen quantification in a predictable fashion.[60–62] One way to address this issue is to find the oxygen and temperature dependence of each PFC separately; this work is currently underway for future application.

In addition to the acquisition of ^{19}F-NMR spectra, PERFUMNs were imaged by ^{1}H and ^{19}F-MRI at 16.4 T. Comparison of the ^{1}H-MRI and ^{19}F-MRI images of PFCE-PERFUMNs shows a decrease in the intensity of ^{19}F signal consistent with the two-fold dilution series (Figure 4). The 4×4 region of interest (ROI) analysis, shows that the signal-to-noise ratio has a linear relationship with the fluorine concentration (Figure S10). The linear regression was a good fit (R^2= 0.95) and the SNR increased by a factor of 2.3 ± 0.3 with change in fluorine concentration. ROI analysis also reveals all clearly visible dilutions have an SNR greater than 10; this is a recommended threshold to overcome at any magnetic field strength.[63] At this magnetic field strength the lowest concentration (0.025 mg/mL, 1.6 mM equivalent ^{19}F nuclei) of PFCE-PERFUMNs was barely visible, indicative that concentrations of PERFUMNs ≥ 0.05 mg/mL with greater than 3.1 mM equivalent ^{19}F nuclei are desirable for further oximetry measurements and imaging.

PERFUMN Oxygen Measurements in Whole Blood

Mesoporous silica nanoparticles are known to be stable in biological environments, especially in the hour timeframe of experiments previously described. [54, 64, 65] To test the feasibility of the PERFUMNs in biologically relevant conditions at long time scales, the oxygen sensitivity of PFCE-PERFUMNs were measured in whole blood. All PFCE-PERFUMN blood measurements were acquired with a 470 MHz at 300 K. Triplicate measurements of PFCE-PERFUMNs reveals the R_1 values were constant up to two days after incubation in whole blood, but started to decrease after three days (Figure S11). In a

second experiment, to measure the sensitivity of PFCE-PERFUMNs to varying oxygen levels, R_1 relaxation rates were measured two days after nanoparticles were added to whole blood and compared to PFCE-PERFUMNs in water. Measurements of R_1 at 0%, 21%, and 100% O_2 reveal a linear dependence, but a 1.6 fold decrease in sensitivity, to oxygen in whole blood relative to water (Figure S12).

Of note, the rabbit blood was not treated with anti-coagulation or anti-inflammatory agents. Potential blood degradation was suggested due to severe discoloration after week long agitation or introduction of anoxic conditions (Figure S13). The potential degradation of the blood sample could have affected the relaxation of the PERFUMNs by decreasing the total blood oxygen content, or causing paramagnetic relaxation effects from the iron in degraded or deoxygenated hemoglobin. However, at least up to two days, it is clear that oxygen measurements are possible in biological samples. The stability of PERFUMNs and the effects on oxygen sensitivity in biological environments will be the focus of future experiments.

Conclusions

In summary, we have reported the use of mesoporous silica nanoparticles loaded with perfluorocarbon small molecules for application to oximetry. These particles feature a comparatively high loading capacity, making it possible to encapsulate a large amount of perfluorocarbons (five times greater than MSNs). Additionally, the post-synthesis loading of PFCs allows for use of broad range of PFC liquids with a single platform nanoparticle carrier. The ability to analytically measure the oxygenation level in biological environments, which was shown feasible in whole blood, is important in the design or improvement of biomedical devices and clinical therapies (*e.g.*, radiation therapy). PERFUMNs are ideal oximetry agents due to their non-invasive NMR-based detection, biologically inert and compatible material, and sensitivity to changes in oxygen levels in microscopic environments. Further exploration of this technology's application in a wide range of settings is underway.

Materials and Methods

Materials

Hexadecyltrimethylammonium bromide (CTAB), Chlorotrimethylsilane (TMSCl), trifluoroacetic acid (TFA), tetraethyl orthosilicate (TEOS), and N,N-dimethylhexadecylamine (DMHA) were purchased from Sigma-Aldrich (St. Lois, MO, USA). The PEG-silane, 2-[methoxy(polyethyleneoxy)9–12propyl]trimethylsilane, was purchased from Gelest, Inc (Morrisville, PA, USA). Decane was purchased from Tokyo Chemical Industry Co., LTD (Toshima, Kitaku, Tokyo, Japan). Perfluoro-15-crown-5-ether (PFCE) was purchased from Exfluor Research Corporation (Round Rock, TX, USA). Perfluorodecalin (PFD) was purchased from Fluoromed L.P (Round Rock, TX, USA). Perfluoro(tert-butylcyclohexane) (PFTBCH) was purchased from Synquest Labs, Inc (Alachua, FL, USA). All chemicals were used without further purification.

Data Analysis

All statistical analyses were performed with Prism version 6.7 (GraphPad Software, San Diego, CA, USA). Quantitative TEM measurements were performed with ImageJ (NIH, USA). Measurements were made by drawing a line segment across the scale bar and setting the pixel/nm scale. The diameter of the particles was measured by using the oval draw tool to fit an ellipse diameter. Unless stated otherwise all quantitative data are expressed as the mean ± standard deviation.

Synthesis of UMNs

UMNs were synthesized via the sol-gel approach as reported previously.[39] Batches of UMNs that were made in triplicate were used to analyze variation in synthesis. In a 20-mL scintillation vial, 0.145 g of CTAB was mixed with 10 mL of ultrapure water, 150 μL of DMHA, and 116 μL of decane. The solutions were stirred with magnetic stir bars at 50 °C for one hour. The solutions were then sonicated for 1–3 hours in a sonication bath (Branson 2510). The rest of the synthesis steps were performed at 50 °C. The sonicated solution was mixed in an Erlenmeyer flask of 150 g, 0.256 M NH_4OH. 2.5 mL of 0.88 M TEOS was added drop-wise and stirred for one hour. The surfaces of the newly formed UMNs were modified by adding 450 μL of PEG, stirring for 30 minutes, and then adding 68 μL of TMSCl in a drop-wise manner. The solutions were aged at 50 °C for 16–18 hours until final volumes were below 50 mL. The particles were then hydrothermally treated by heating solutions within a glass media bottle in a 90 °C oven for 24 hours.[66]

At 24 hours, the solutions were removed from the oven and vacuum filtered. The solutions were centrifuged several times for 35 minutes at 4 °C and 66,000 × g (Beckman Coulter Optima L-100K) with two intermediate ion-exchange steps in a reflux apparatus. The CTAB was removed in the ion-exchange steps by dispersing UMN pellets in 6 g/L NH_4NO_3 (dissolved in 190 proof ethanol) and stirring solutions in a 100-mL round bottom flask at 50 °C for one hour. Ion exchange washes were followed by washes with 190 proof ethanol. UMNs were washed once in 200 proof ethanol then redispersed in 200 proof ethanol. Final solutions of UMN were filtered through 5-μm Versapor membrane syringe filters (Pall Co., Radnor, PA) to remove hair and dust particles.

Loading and Extraction of PERFUMNs

PERFUMNs were made by loading UMNs with different types of PFCs: PFCE, PFD, or PFTBCH. UMN synthesis replicates were loaded in triplicate to analyze the variation in loading. UMNs were dried from 200 proof ethanol at 10 Torr, 21°C, for one hour. The mass to volume ratio of UMNs to PFC liquid was kept at a range of 3–4 (*e.g.*, 10 mg UMN/ 3 mL PFC). UMNs were added to liquid PFCs at room temperature in Nalgene™ centrifuge tubes. The colloid solution was shaken by hand, and then sonicated for 10 minutes in a sonication bath. After sonication, the PERFUMNs were extracted in ultrapure water (pH ≤ 7.4) by adding an equal volume of water to PFC and vortexing the phases for 10 seconds. The opacity of the aqueous phase became turbid after complete phase separation. The washing step was performed two or three more times as needed; ultrapure water was added to the solution to make the final volume equal to the mass of nanoparticles (*i.e.*, 1 mg/mL). The concentration of nanoparticles was determined by drying 3 mL aliquots in a 20-mL

scintillation vial at 10 Torr, 40 °C, for one hour. The difference in mass of the vial before and after was used to calculate the mass of nanoparticles in solution.

Materials Characterization

The hydrodynamic diameter and zeta potential of the nanoparticles were measured by dynamic light scattering (DLS, Brookhaven BIC ZetaPals), with a 35 mW 660 nm laser at room temperature. The zeta potential was measured in ultrapure water with a Brookhaven ZetaPALS Zeta-Potential Analyzer (Holtsville, NY). Particle porosity and surface area were measured with N_2 Physisorption (Micromeritics ASAP 2020, GA, USA). Samples were then analyzed under the ASAP 2020 analysis port at cryogenic temperatures. The surface area and pore size of samples were determined by the BJH method. Electron micrographs of the UMNs and PERFUMNs were obtained *via* TEM (FEI Tecnai 12, Houston, TX, USA) and Cryo-TEM (Tecnai G2 Spirit Biotwin, Houston, TX, USA) respectively. In TEM, 3 μL of UMNs were dried on Formvar-coated carbon grids overnight. For Cryo-TEM, 3 μL of PERFUMNs were placed on lacey carbon grids which were immediately dried with filter paper for 5 seconds at 100% humidity. The samples were vitrified by submerging grids into liquid ethane. Electron micrographs were obtained at 120 kV with an emission current of 4 mA.

^{9}F-NMR Quantification

All NMR spectra were obtained at 470 MHz on a Bruker Avance III 500 MHz instrument equipped with a 5 mm Prodigy TCI Cryoprobe. Samples were prepared with 5% D_2O and 52 μM trifluoroacetic acid (-76.5 ppm) as a reference and calibration standard to calculate loading values. Loaded nanoparticle solutions were vortexed for 0.5 to 1 min immediately prior to mixing with D_2O and TFA. NMR tubes were vortexed for 30 s within 10 min. prior to acquisition of NMR spectra. Parameters for ^{19}F NMR experiments included an 8.5 s delay time and a 2 s acquisition time (AQ), to allow for complete relaxation of magnetization following a full 90 degree pulse. For PFD, spectral width and offset were 80 and −110 ppm, respectively. For PFCE, spectral width and offset were 30 and −85 ppm, respectively. For PFTBCH, spectral width and offset were 25 and −67 ppm, respectively. PFC loading was calculated by comparing relative integrations of select resonances from the PFC to TFA. T_1 relaxation times were measured using the inversion recovery method at 470 MHz and 300 K, for determining optimal delay times to allow for quantitative measurement of each fluorine resonance. These measurements were performed under standard atmospheric condition.

^{19}F-MRS Oxygen Sensitivity

^{19}F spectra and images were acquired with a 16.4 T (700 MHz) MR system (Agilent Technologies, Santa Clara, CA, USA) using a custom-built single-loop surface coil (2.5 cm diameter) tuned to 656.8 MHz. Oximetry and thermometry methods were previously described for neat compounds.[57] Briefly, the selected PERFUMN was suspended in water and pipetted into a 2-mL vial. The vial was centered in the coil; the coil was tuned, and inserted into the isocenter of the magnet. PFCs have been known to saturate with a gas after 15 minutes.[25, 26] The sample was then bubbled and equilibrated with a gas of known oxygen concentration for 30 minutes (as previously verified with a calibrated 250 μm fluorescence-quenching fiber optic [FO] probe [Ocean Optics, Dunedin, FL, USA]) while the temperature

was held constant. Temperature was monitored with an additional FO probe and was maintained using a forced-air heater and water circulator. The magnet was shimmed and R_1 ($1/T_1$) was then measured with a standard inversion-recovery pulse sequence with customized delay times optimized to each sample's R_1.[67, 68] PFCE benefits from processing only a single resonance, but for PFD and PFTBCH (which have multiple resonances) the I[69] and major (described above) resonances, respectively, were interrogated. R_1 measurements were made for five different oxygen concentrations (0, 38, 76, 114, and 160 mmHg) at three different temperatures (21, 37, and 45 degrees C). Each condition was measured in replicate (N=2–6) with a repetition time of at least $5/R_1$. R_1 was assumed linear with both oxygen concentration and temperature as previously described.[30, 57, 61]

MRI Phantom Images

Samples of UMN and PERFUMNs loaded with PFCE were transferred to 6 mm culture tubes. These tubes were vertically centered within a 2.5 cm diameter surface coil for imaging. The central tube was the unloaded UMN at 1 mg/mL. A completely empty tube was included in the outer ring of samples between the highest and lowest PERFUMN concentration (0.03 mg UMN/mL and 0.09 mM PFCE). The ^{19}F and ^{1}H images were both acquired using a gradient echo pulse sequence with a resolution of 0.78×0.78 mm at 16.4 T. The ^{19}F image was acquired with the following settings: slice thickness = 10 mm; repetition time (TR) = 400 ms; echo time (TE) = 2.0 ms; flip angle = 90°; 64 averages, acquisition time (AQ) = 3.23 ms; receiver bandwidth (sw) = 19841 Hz; data matrix = 64×64; and FOV = 50×50 mm. The measurement took 27.3 minutes. The ^{1}H image was acquired with the following settings: slice thickness = 5 mm; TR = 40 ms; TE = 0.78 ms; flip angle = 2°; 1 average; AQ = 0.15 ms; sw = 208333 Hz; data matrix = 32×32; and FOV = 25×25 mm. The measurement took 1.3 s.

Rabbit Blood Oximetry

Rabbit New Zealand White blood was provided by Bakkom Rabbitry. In the first week, triplicate samples were made by placing 2.5 mL of rabbit blood in a round bottom polystyrene culture tube with a snap cap. Three tubes with 8 mL of PFCE-PERFUMNs were centrifuged for 12 minutes at 22 °C and 66,000 × g. A soft pellet was formed and 7 mL of supernatant were removed from the tubes. The remaining 1 mL of PFCE-PERFUMNs was vortexed for 20 seconds, until well mixed, and then added to the tube of rabbit blood. The treated rabbit blood was agitated on a benchtop rocking table at room temperature. Each day 475 μL of blood were added to NMR tubes with 25 μL of D_2O. All ^{19}F-NMR measurements were obtained at 470 MHz on a Bruker Avance III 500 MHz instrument at 300 K. T_1 relaxation times were measured using a standard inversion recovery method with time points ranging from 0.010 s to 8 s, an acquisition time of 2 s, and delay time of 6 s.

In the second week 2.5 mL of fresh rabbit blood were placed in the culture tubes. Without centrifugation, 1 mL of PFCE-PERFUMNs from stock were added to the rabbit blood. The blood was placed on the benchtop rocking table at room temperature. Two days after the PERFUMNs were added, 475 μL of treated blood were placed into three J-Young NMR tubes, with 25 μL of D_2O, each. One tube was aerated with 100% O_2 and the other was aerated with 100% N_2. Both tubes were aerated for 30 minutes, and the headspace above the

blood was subsequently filled with the corresponding gas to maintain an oxygen or nitrogen rich environment. The third tube was left open to atmospheric air. The T_1 relaxation times of these samples were measured as described above.

Supplementary Material

Refer to Web version on PubMed Central for supplementary material.

Acknowledgments

This work was supported in part by the Minnesota Lions Diabetes Foundation, the Schott Family Foundation, the Carol Olson Memorial Diabetes Research Fund, and the NIH grants P41 EB015894 and S10 RR025031. Parts of this work were carried out in the Characterization Facility, University of Minnesota, a member of the NSF-funded Materials Research Facilities Network (www.mrfn.org) *via* the MRSEC program. Rabbit blood was properly collected under IACUC Protocol 1610-34243A by Ellorie R. Liljequist, Bakkom Rabbitry. Special thanks to members of the Lu Lab, University of Minnesota, for providing the gasses and apparatus to conduct oximetry studies in blood. A. Lee would like to acknowledge the NIH chemistry-biology interface training grant 5T32GM008700-18 and the University of Minnesota's Diversity of Views and Experiences Fellowship for funding. C. Gee would like to acknowledge the NIH chemistry–biology interface training grant T32-GM08700 and the University of Minnesota Interdisciplinary Doctoral Dissertation Fellowship for funding. A. Juelfs would like to acknowledge the University of Minnesota Undergraduate Research Opportunities Program for funding. The authors also thank Dr. Lynn E. Eberly for statistical analysis consultation.

ABBREVIATIONS

CTAB	cetyltrimethylammonium bromide
CV	coefficient of variation
DMHA	dimethylhexadecylamine
HFB	hexafluorobenzene
MSNs	mesoporous silica nanoparticles
PERFUMNs	perfluorocarbon-loaded UMNs
PFC	perfluorocarbon
PFCE	perfluoro-15-crown-5-ether
PFD	perfluorodecalin
PFOB	perfluorooctyl bromide
PFTBA	perfluorotributylamine
PFTBCH	perfluorotributylcyclohexane
TEOS	tetraethyl orthosilicate
TFA	trifluoroacetic acid
TMSCl	chlorotrimethylsilane
UMNs	ultraporous mesostructured silica nanoparticles.

References

1. Lau J, Henriksnas J, Svensson J, Carlsson PO. Oxygenation of Islets and its Role in Transplantation. Curr. Opin. Organ Transplant. 2009; 14:688–693. [PubMed: 19745734]
2. Corry, RJ., Shapiro, R. Pancreatic Transplantation. Informa Healthcare; New York: 2007.
3. Morinet F, Casetti L, Francois JH, Capron C, Pillet S. Oxygen Tension Level and Human Viral Infections. Virology. 2013; 444:31–36. [PubMed: 23850460]
4. Diepart C, Verrax J, Calderon PB, Feron O, Jordan BF, Gallez B. Comparison of Methods for Measuring Oxygen Consumption in Tumor Cells. In Vitro. Anal. Biochem. 2010; 396:250–256. [PubMed: 19766582]
5. Deleo, F., Otto, MW. Bacterial Pathogenesis: Methods and Protocols. Humana Press; Totowa, N.J: 2008.
6. Bennewith KL, Dedhar S. Targeting Hypoxic Tumour Cells to Overcome Metastasis. BMC Cancer. 2011; 11:504. [PubMed: 22128892]
7. Sun JD, Liu Q, Wang Jl, Ahluwalia D, Ferraro D, Wang Y, Duan J, Ammons W, Curd J, Matteucci MD, Hart CP. Selective Tumor Hypoxia Targeting by Hypoxia-Activated Prodrug TH-302 Inhibits Tumor Growth in Preclinical Models of Cancer. Clin. Cancer Res. 2012; 18:758–770. [PubMed: 22184053]
8. Rischin D, Mileshkin L, Narayan K, Bernshaw D, Oza AM, Choi J, McClure B, Hicks R, Fyles A. Phase 1 Study of Tirapazamine in Combination with Radiation and Weekly Cisplatin in Patients with Locally Advanced Cervical Cancer. Int. J. Gynecol. Cancer. 2010; 20:827–833. [PubMed: 20606530]
9. Tatum JL. Hypoxia: Importance in Tumor Biology, Noninvasive Measurement by Imaging, and Value of Its Measurement in the Management of Cancer Therapy. Int. J. Radiat. Biol. 2006; 82:699–757. [PubMed: 17118889]
10. Ortega R, Hansen CJ, Elterman K, Woo A. Pulse Oximetry. N. Engl. J. Med. 2011; 364
11. Vikram DS, Zweier JL, Kuppusamy P. Methods for Noninvasive Imaging of Tissue Hypoxia. Antioxid. Redox Signal. 2007; 9:1745–1756. [PubMed: 17663644]
12. Krohn KA, Link JM, Mason RP. Molecular Imaging of Hypoxia. J. Nucl. Med. 2008; 49:129–148. [PubMed: 18077531]
13. Fuchs J, Groth N, Herrling T, Milbradt R, Zimmer G, Packer L. Electron Paramagnetic Resonance (EPR) Imaging in Skin: Biophysical and Biochemcial Microscopy. J. Invest. Dermatol. 1992; 98:713–719. [PubMed: 1314866]
14. Swartz HM, Williams BB, Zaki BI, Hartford AC, Jarvis LA, Chen EY, Comi RJ, Ernstoff MS, Hou H, Khan N, Swarts SG, Flood AB, Kuppusamy P. Clinical EPR: Unique Opportunities and Some Challenges. Acad. Radiol. 2014; 21:197–206. [PubMed: 24439333]
15. O'Hara JA, Khan N, Hou H, Wilmot CM, Demidenko E, Dunn JF, Swartz HM. Comparison of EPR Oximetry and Eppendorf Polarographic Electrode Assessments of Rat Brain PtO_2. Physiol. Meas. 2004; 25:1413–1423. [PubMed: 15712720]
16. Sundramoorthy SV, Epel B, Halpern HJ. Orthogonal Resonators for Pulse *In Vivo* Electron Paramagnetic Imaging at 250 MHz. J. Magn. Reson. 2014; 240:45–51. [PubMed: 24530507]
17. Salikhov I, Walczak T, Lesniewski P, Khan N, Iwasaki A, Comi R, Buckey J, Swartz HM. EPR Spectrometer for Clinical Applications. Magn. Reson. Med. 2005; 54:1317–1320. [PubMed: 16193470]
18. Riess JG, Krafft MP. Advanced Fluorocarbon-Based Systems for Oxygen and Drug Delivery, and Diagnosis. Artif. Cells Blood Substit. Immobil. Biotechnol. 1997; 25:43–52. [PubMed: 9083625]
19. Ruiz-Cabello J, Walczak P, Kedziorek DA, Chacko VP, Schmieder AH, Wickline SA, Lanza GM, Bulte JWM. In Vivo “Hot Spot” MR Imaging of Neural Stem Cells Using Fluorinated Nanoparticles. Magn. Reson. Med. 2008; 60:1506–1511. [PubMed: 19025893]
20. Partlow KC, Chen J, Brant JA, Neubauer AM, Meyerrose TE, Creer MH, Nolta JA, Caruthers SD, Lanza GM, Wickline SA. ^{19}F Magnetic Resonance Imaging for Stem/Progenitor Cell Tracking with Multiple Unique Perfluorocarbon Nanobeacons. FASEB J. 2007; 21:1647–1654. [PubMed: 17284484]

21. Ruiz-Cabello J, Barnett BP, Bottomley PA, Bulte JWM. Fluorine ^{19}F MRS and MRI in Biomedicine. NMR Biomed. 2011; 24:114–129. [PubMed: 20842758]
22. Dhawan, AP. Medical Image Analysis. IEEE Press; John Wiley & Sons, Inc; Piscataway, NJ; Hoboken, New Jersey: 2011.
23. Yu JX, Hallac RR, Chiguru S, Mason RP. New Frontiers and Developing Applications in ^{19}F NMR. Prog. Nucl. Magn. Reson. Spectrosc. 2013; 70:25–49. [PubMed: 23540575]
24. Brabets R, Clark D, Snelson A. Solubility of Ozone in Some Flourocarbon Solvents. J. Fluorine Chem. 1988; 41:311–320.
25. Wesseler EP, Iltis R, Clark LC Jr. The Solubility of Oxygen in Highly Fluorinated Liquids. J. Fluorine Chem. 1977; 9:137–146.
26. Sharts CM, Reese HR, Ginsberg KA, Multer FK, Nielson MD, Greenburg AG, Peskin GW, Long DM. The Solubility of Oxygen in Aqueous Fluorocarbon Emulsions. J. Fluorine Chem. 1978; 11:637–641.
27. Riess JG, Krafft MP. Fluorinated Materials for *In Vivo* Oxygen Transport (Blood Substitutes), Diagnosis and Drug Delivery. Biomaterials. 1998; 19:1529–1539. [PubMed: 9794531]
28. Krafft MP, Riess JG. erfluorocarbons: Life Sciences and Biomedical Uses Dedicated to the Memory of Professor Guy Ourisson, a True Renaissance Man. J. Polym. Sci., Part A: Polym. Chem. 2007; 45:1185–1198.
29. Riess JG. Understanding the Fundamentals of Perfluorocarbons and Perfluorocarbon Emulsions Relevant to *In Vivo* Oxygen Delivery. Artif. Cells Blood Substit. Immobil. Biotechnol. 2005; 33:47–63. [PubMed: 15768565]
30. Parhami P, Fung P. Fluorine-19 Relaxation Study of Perfluorochemicals as Oxygen Carriers. J. Phys. Chem. 1983; 87:1928–1931.
31. Mahon RT, Auker CR, Bradley SG, Mendelson A, Hall AA. The Emulsified Perfluorocarbon Oxycyte Improves Spinal Cord Injury in a Swine Model of Decompression Sickness. Spinal Cord. 2012; 51:188–192. [PubMed: 23165506]
32. Yacoub A, Hajec MC, Stanger R, Wan W, Young H, Mathern BE. Neuroprotective Effects of Perflurocarbon (Oxycyte) After Contusive Spinal Cord Injury. J. Neurotrauma. 2014; 31:256. [PubMed: 24025081]
33. LoNostro P, Choi SM, Ku CY, Chen SH. Fluorinated Microemulsions: A Study of the Phase Behavior and Structure. J. Phys. Chem. B. 1999; 103:5347–5352.
34. Oda R, Huc I, Danino D, Talmon Y. Aggregation Properties and Mixing Behavior of Hydrocarbon, Fluorocarbon, and Hybrid Hydrocarbon Fluorocarbon Cationic Dimeric Surfactants. Langmuir. 2000; 16:9759–9769.
35. Freire MG, Dias AMA, Coelho MAZ, Coutinho JAP, Marrucho IM. Aging Mechanisms of Perfluorocarbon Emulsions Using Image Analysis. J. Colloid Interface Sci. 2005; 286:224–232. [PubMed: 15848420]
36. Grapentin C, Barnert S, Schubert R. Monitoring the Stability of Perfluorocarbon Nanoemulsions by Cryo-TEM Image Analysis and Dynamic Light Scattering. PLoS ONE. 2015; 10
37. Chin LS, Lim M, Hung TT, Marquis CP, Amal R. Perfluorodecalin Nanocapsule as an Oxygen Carrier and Contrast Agent for Ultrasound Imaging. RSC Adv. 2014; 4:13052–13060.
38. Nakamura T, Sugihara F, Matsushita H, Yoshioka Y, Mizukami S, Kikuchi K. Mesoporous Silica Nanoparticles for ^{19}F Magnetic Resonance Imaging, Fluorescence Imaging, and Drug Delivery. Chem. Sci. 2015; 6:1986–1990. [PubMed: 28706648]
39. Egger SM, Hurley KR, Datt A, Swindlehurst G, Haynes CL. Ultraporous Mesostructured Silica Nanoparticles. Chem. Mater. 2015; 27:3193–3196.
40. Pope EJA, Mackenzie JD. Sol-Gel Processing of Silica. J. Non Cryst. Solids. 1986; 87:185–198.
41. Essien E, Olaniyi O, Adams L, Shaibu R. Sol-Gel-Derived Porous Silica: Economic Synthesis and Characterization. JMMCE. 2012; 11:976–981.
42. Rao, CNR., Biswas, K. Essentials of Inorganic Materials Synthesis. John Wiley & Sons, Inc; Hoboken, New Jersey: 2015.
43. Lin YS, Hurley KR, Haynes CL. Critical Considerations in the Biomedical Use of Mesoporous Silica Nanoparticles. J. Phys. Chem. Lett. 2012; 3:364. [PubMed: 26285853]

44. Lin YS, Haynes CL. Impacts of Mesoporous Silica Nanoparticle Size, Pore Ordering, and Pore Integrity on Hemolytic Activity. J. Am. Chem. Soc. 2010; 132:4834. [PubMed: 20230032]
45. Nobbmann, U. Polydispersity: What Does it Mean for DLS and Chromatography?. http://www.materials-talks.com/blog/2014/10/23/ polydispersity-what-does-it-mean-for-dls-and-chromatography/
46. Alothman AZ. A Review: Fundamental Aspects of Silicate Mesoporous Materials. Materials. 2012; 5
47. Thommes M, Kaneko K, Neimark A, Olivier JP, Rodriguez-Reinoso F, Rouquerol J, Sing K. Physisorption of Gases, with Special Reference to the Evaluation of Surface Area and Pore Size Distribution (IUPAC Technical Report). Pure Appl. Chem. 2015; 87:1051–1069.
48. Bootz A, Vogel V, Schubert D, Kreuter J. Comparison of Scanning Electron Microscopy, Dynamic Light Scattering and Analytical Ultracentrifugation for the Sizing of Poly(butylcyanoacrylate) Nanoparticles. Eur. J. Pharm. Biopharm. 2004; 57:369–375. [PubMed: 15018998]
49. Carter, CB., Williams, DB. Transmission Electron Microscopy: Diffraction, Imaging, and Spectrometry. Springer; Switzerland: 2016.
50. Berg, JC. An Introduction to Interfaces & Colloids: The Bridge to Nanoscience. World Scientific; Hackensack, N.J: 2010.
51. Anderson W, Kozak D, Coleman VA, Jamting AK, Trau M. A Comparative Study of Submicron Particle Sizing Platforms: Accuracy, Precision and Resolution Analysis of Polydisperse Particle Size Distributions. J. Colloid Interface Sci. 2013; 405:322–330. [PubMed: 23759321]
52. Jacoby C, Temme S, Mayenfels F, Benoit N, Krafft MP, Schubert R, Schrader J, Flogel U. Probing Different Perfluorocarbons for *In Vivo* Inflammation Imaging by ^{19}F MRI: Image Reconstruction, Biological Half-Lives and Sensitivity. NMR Biomed. 2014; 27:261–271. [PubMed: 24353148]
53. Bezinover D, Ramamoorthy S, Uemura T, Kadry Z, Mcquillan PM, Mets B, Falcucci O, Rannels S, Ruiz-Velasco V, Spiess B, Liang J, Mani H, Lou X, Janicki PK. Use of a Third-Generation Perfluorocarbon for Preservation of Rat DCD Liver Grafts. J. Surg. Res. 2012; 175:131–137. [PubMed: 21543088]
54. Matsushita H, Mizukami S, Sugihara F, Nakanishi Y, Yoshioka Y, Kikuchi K. Multifunctional Core-Shell Silica Nanoparticles for Highly Sensitive ^{19}F Magnetic Resonance Imaging. Angew. Chem. Int. Ed. 2014; 53:1008–1011.
55. Huang X, Li L, Liu T, Hao N, Liu H, Chen D, Tang F. The Shape Effect of Mesoporous Silica Nanoparticles on Biodistribution, Clearance, and Biocompatibility. In Vivo. ACS Nano. 2011; 5:5390–5399. [PubMed: 21634407]
56. Dardzinski BJ, Sotak CH. Rapid Tissue Oxygen Tension Mapping Using ^{19}F Inversion-Tecovery Echo-Planar Imaging of Perfluoro-15-crown-5-ether. Magn. Reson. Med. 1994; 32:88–97. [PubMed: 8084241]
57. Einstein SA, Weegman BP, Firpo MT, Papas KK, Garwood M. Development and Validation of Noninvasive Magnetic Resonance Relaxometry for the *In Vivo* Assessment of Tissue-Engineered Graft Oxygenation. Tissue Eng. 2016; 22:1009–1017.
58. Kuethe DO, Montaño R, Pietra T. Measuring Nanopore Size from the Spin-Lattice Relaxation of CF_4 Gas. J. Magn. Reson. 2007; 186:243–251. [PubMed: 17400493]
59. Nakamura T, Matsushita H, Sugihara F, Yoshioka Y, Mizukami S, Kikuchi K. Activatable ^{19}F MRI Nanoparticle Probes for the Detection of Reducing Environments. Angew. Chem. Int. Ed. 2015; 54:1007–1010.
60. Thomas SR, Pratt RG, Millard RW, Samaratunga RC, Shiferaw Y, McGoron AJ, Tan KK. In Vivo pO2 Imaging in the Porcine Model with Perfluorocarbon ^{19}F NMR at Low Field. Magn. Reson. Imaging. 1996; 14:103–114. [PubMed: 8656982]
61. Mason RP, Shukla H, Antich PP. *In Vivo* Oxygen Tension and Temperature: Simultaneous Determination Using ^{19}F NMR Spectroscopy of Perfluorocarbon. Magn. Reson. Med. 1993; 29:296–302. [PubMed: 8450738]
62. Shukla HP, Mason RP, Bansal N, Antich PP. Regional Myocardial Oxygen Tension: ^{19}F MRI of Sequestered Perfluorocarbon. Magn. Reson. Med. 1996; 35:827–833. [PubMed: 8744009]
63. Zhao D, Jiang L, Mason RP. Measuring Changes in Tumor Oxygenation. Meth. Enzymol. 2004; 386:378–418. [PubMed: 15120262]

64. Lin YS, Abadeer N, Haynes CL. Stability of Small Mesoporous Silica Nanoparticles in Biological Media. Chem. Commun. 2010; 47:532–534.

65. Huang X, Meng X, Tang F, Li L, Chen D, Liu H, Zhang Y, Ren J. Mesoporous Magnetic Hollow Nanoparticles—Protein Carriers for Lysosome Escaping and Cytosolic Delivery. Nanotechnology. 2008; 19:445101. [PubMed: 21832718]

66. Lin YS, Abadeer N, Hurley KR, Haynes CL. Ultrastable, Redispersible, Small, and Highly Organomodified Mesoporous Silica Nanotherapeutics. J. Am. Chem. Soc. 2011; 133:20444–20457. [PubMed: 22050408]

67. Bernassau JM, Hyafil F. Choice of Delay Time Sequence in Spin-Lattice Relaxation Time Measurements by Inversion- Recovery. J. Magn. Reson. 1980; 40:245–258.

68. Weiss GH, Ferretti JA. Optimal Design of Relaxation Time Experiments. Prog. Nucl. Magn. Reson. Spectrosc. 1988; 20:317–335.

69. Fung BM. Selective Detection of Multiplets *via* Double Quantum Coherence: A ^{19}F NMR Study of Perfluorodecalin. Org. Magn. Reson. 1983; 21:397–398.

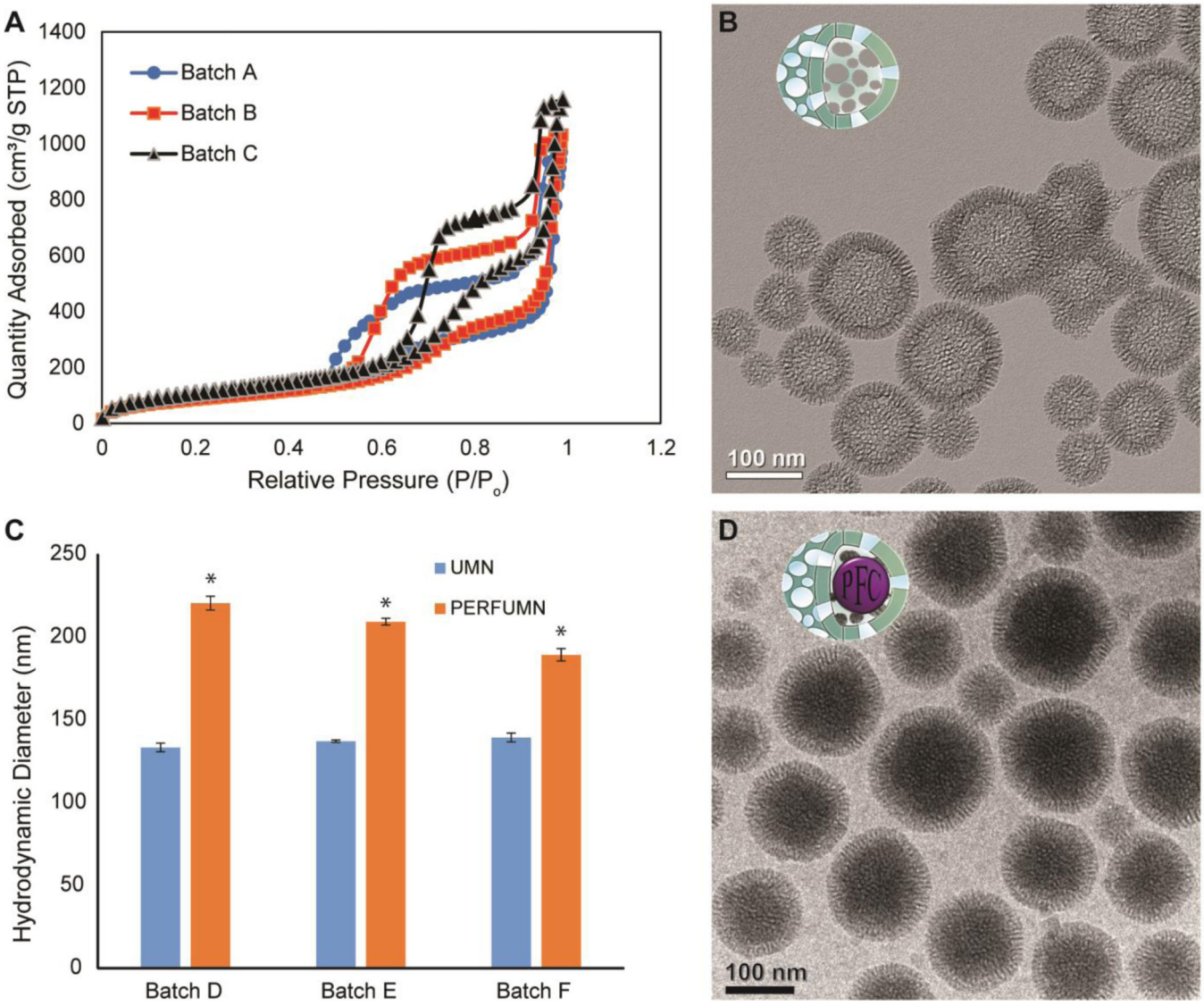

Figure 1.

Characterization data and images of nanoparticles. A) N_2 physisorption data from replicate unloaded nanoparticle batches showing type IV isotherms with a type 5 hysteresis (H5) loop. B) TEM image of unloaded nanoparticles with hollow lacey cavities surrounded by silica wall with average thickness of 22 ± 1 nm (mean ± SEM). C) Triplicate, pair-wise, DLS diameter comparison between UMNs and PFCE-PERFUMNs; error bars are the standard error; PERFUMNs are statistically (* = $p < 0.05$) distinguishable from the unloaded nanoparticles. D) Cryo-TEM image of PERFUMNs; the previously hollow cavities now show a change in mass-thickness contrast, indicating the nanoparticles are packed by atomically heavy PFCs.

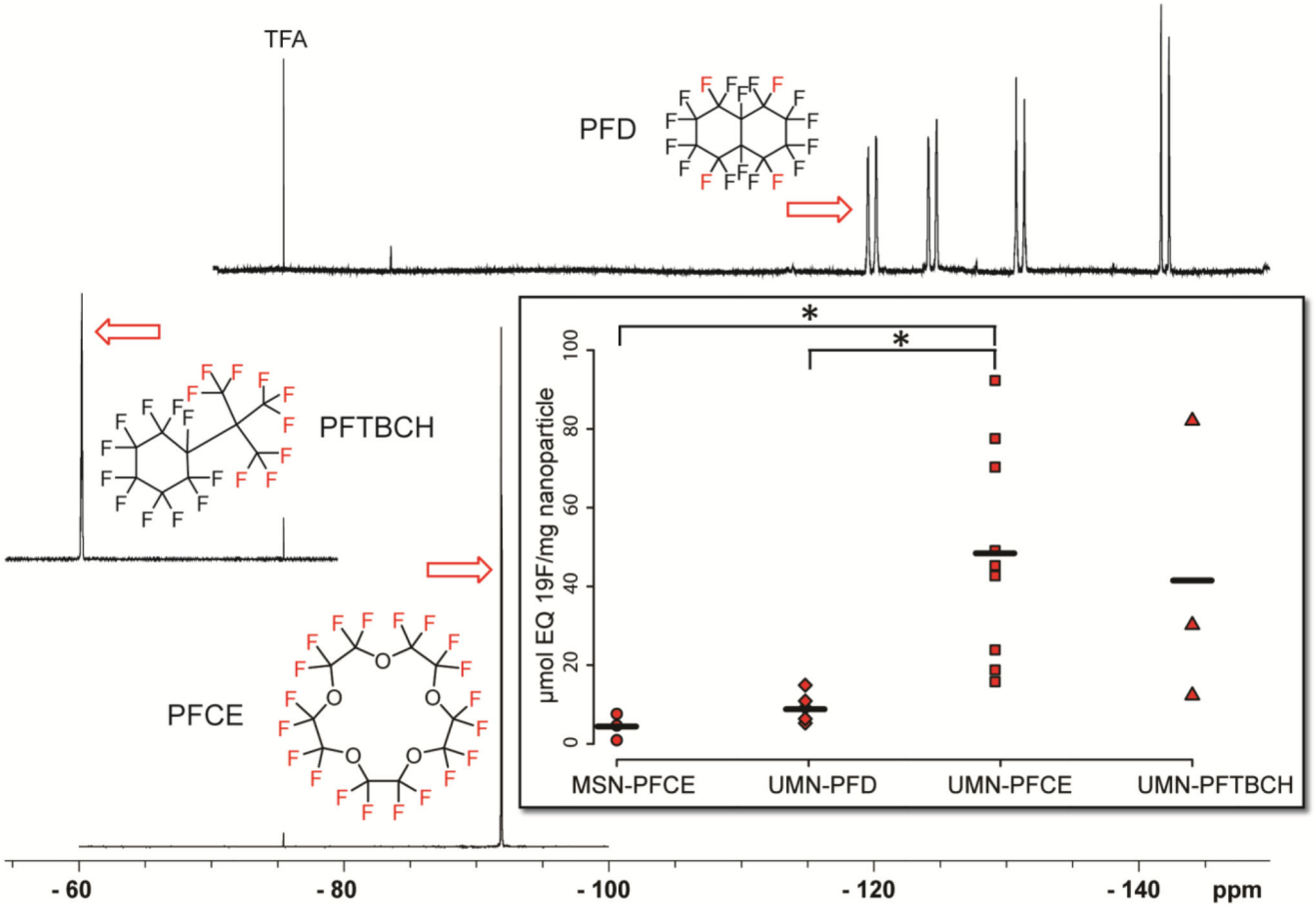

Figure 2.

Stacked ^{19}F-NMR spectra of three different PERFUMNs with the equivalent fluorines used for quantification shown in red. All spectra are referenced to TFA at −76.5 ppm. Inset) PFC loading comparison with MSN particles (circle) and the three type of PERFUMNs (PFD = diamond, PFCE = square, PFTBCH = triangle). The strip chart reveals the spread of the data around the mean (black line). The total numbers are 3:6:9:3 going from left to right. The perfluorochemical loading for PFCE-PERFUMNs is significantly higher than PFD-PERFUMNs and PFCE loaded MSNs (* = $p < 0.05$). Loading of PFTBCH-PERFUMNs are indistinguishable from the other samples.

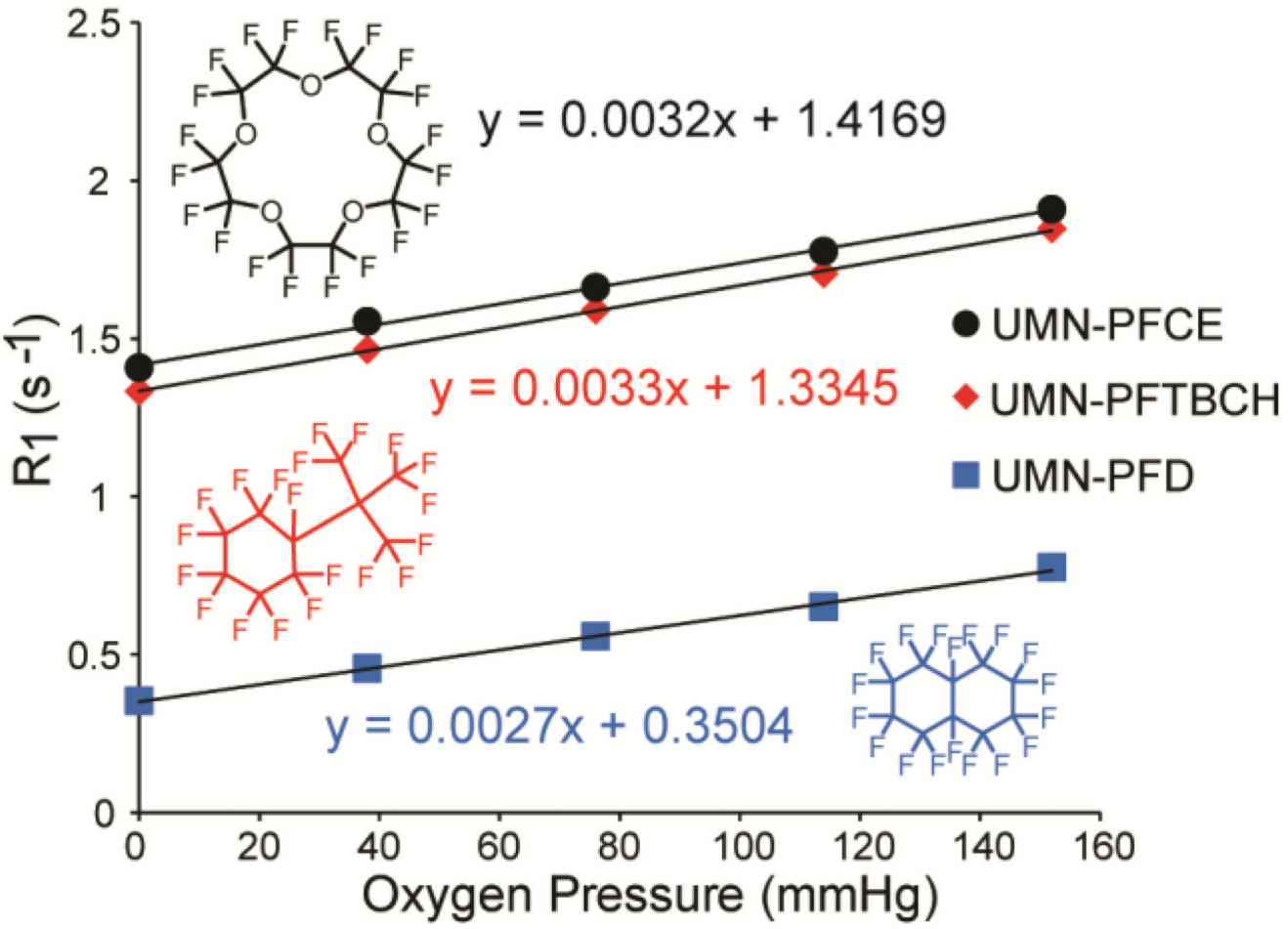

Figure 3.

Oxygen dependence of R_1 values for different PERFUMNs, demonstrating the linear relationship between R_1 and O_2 partial pressures in all three cases. PERFUMNs were measured at 656.8 MHz (16.4 T) at room temperature. Error bars from triplicate measurements are too small to be visible on this graph.

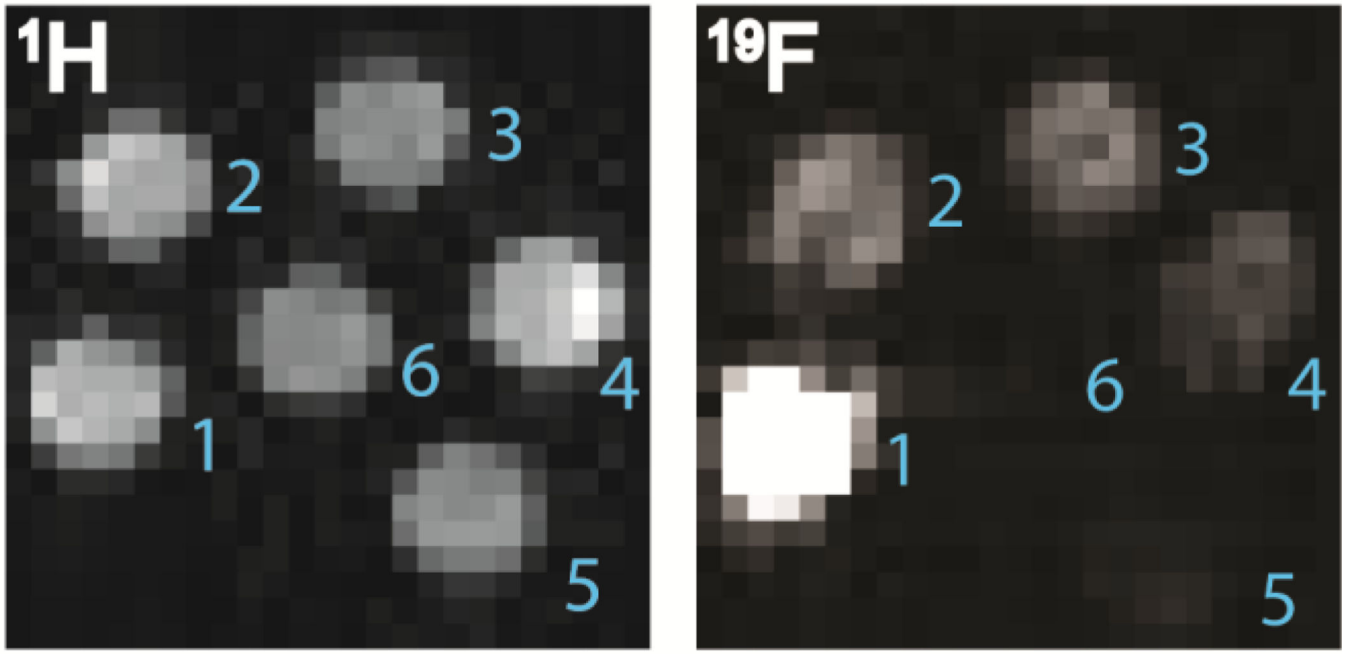

Figure 4.

MRI phantom images of a PFCE-PERFUMN two-fold dilution series acquired at 657 MHz (16.4 T) and room temperature. ^{1}H and ^{19}F images were acquired in 1.3 s and 27.3 min respectively. Left) ^{1}H-MRI image. Right) ^{19}F-MRI image. Concentration of equivalent ^{19}F nuclei in 0.8 mL: 1) 24.8 mM (0.4 mg/mL); 2) 12.4 mM (0.2 mg/mL); 3) 6.2 mM (0.1 mg/mL); 4) 3.1 mM (0.05 mg/mL); 5) 1.6 mM (0.025 mg/mL); 6) 0 mM (1 mg/mL UMN).

Table 1

Physical Characteristics of Dual-Modified UMNs

Parameter	Estimated Value[a]	SD[b]	Confidence Interval (0.95)[c]
Hydrodynamic Diameter (nm)	142	± 33	± 21
Polydispersity	0.11	± 0.06	± 0.04
BJH Surface Area (m^2/g)	532.4	± 74.9	± 41.5
BJH Pore Volume (cm^3/g)	1.8	± 0.3	± 0.7
BJH Pore Size (nm)	13.2	± 1.3	± 12.9

[a] All estimate values are means of the sample distributions.

[b] Standard deviation.

[c] The 95% confidence interval, n=15.